Thermal monitoring of braking systems using metal AM calipers with integrated sensors

X ECCOMAS Thematic Conference on Smart Structures and Materials
SMART 2023
D.A. Saravanos, A. Benjeddou, N. Chrysochoidis and T. Theodosiou (Eds)

THERMAL MONITORING OF BRAKING SYSTEMS USING METAL AM CALIPERS WITH INTEGRATED SENSORS

GIORGIO DE PASQUALE

Smart Structures and Systems Lab, Department of Mechanical and Aerospace Engineering
Politecnico di Torino
Corso Duca degli Abruzzi 24, 10129 Torino, Italy
e-mail: giorgio.depasquale@polito.it, www.giorgiodepasquale.com

Abstract. The incorporation of sensors into mechanical components is experiencing growing capabilities, thanks to emerging fabrication technologies such as metal additive manufacturing (AM). The functionalization of components with sensors has several applications in structural and performance monitoring, as well as failure prediction in prognostics and diagnostics operations. In this paper, a customized laser powder bed fusion (L-PBF) process is developed for embedding stand-alone sensors (and/or electronics, connectors, cables, etc.) into metal parts during the AM growth process. The method is based on interrupting and restarting the micromelting process after the sensor has been positioned. Finally, the integration process is used to fabricate a brake caliper with an embedded thermal sensor. The sensing performance is then validated on the assembled hydraulic braking system, with the aim of monitoring the thermal profile in working conditions.

Key words: Structural Monitoring, Additive Manufacturing, Thermal Sensing, Sensors Integration, Numerical Modeling, L-PBF.

1 INTRODUCTION

The advantages of integrating sensors into AM parts have been discussed for a long time. In [1], the integration of optical fibers with Bragg gratings into metal parts to measure temperature and strain is discussed in depth. In addition to concepts based on structural polymers, the use of laser powder bed fusion (L-PBF) on metal powder is also considered in [2]. In particular, the authors discuss RFID (radio frequency identification) electronic elements embedded in metal components for sensing purposes. In [3], the authors provide a functional design scenario to demonstrate the added value of sensing elements integrated via AM in widely used metal components. Several sensors are considered, including switches, voltage dividers, capacitors, and smart material transducers. The components described include ball bearings, gears, hinges, and screws. In [4], the authors describe a general method for the design and integration of sensors and actuators in Ti6Al4V parts produced with AM. The L-PBF process is used to integrate an electric coil that can be used as a sensor or actuator into a femoral hip stem. The strategy based on cavity creation is applied. Binder et al. [5] present design concepts suitable for integrating sensors in metal components from the L-PBF process. The standard method

proposed is based on process interruption, creation of a cavity, removal of powder, insertion of the sensor, and continuation of the growth process. The case study of PT100 thermocouple integration is presented. The design and prototype of a mechatronic system for the automatic integration of sensors in the L-PBF process are presented in [6, 7]. The system is intended as an integration of the AM machine and allows powder cleaning into the cavity, component pick-up, and placement. The main design specifications and constraints are identified, especially for serial production.

The interruption of the AM process can potentially affect the material's metallographic structure and mechanical properties. Numerous studies have investigated the effects of micromelting interruption and re-start on various materials. For instance, in electron beam melting (EBM), infrared imaging techniques are used to reduce registration error by re-positioning metal parts after process interruption, as described in [8]. However, the vacuum pressure and high temperature in the building chamber make this process challenging. In [9], the effects of L-PBF process interruption on 316L steel are studied, revealing that sample failure is not associated with the material's transition zone. Similarly, [10] investigates the effects of process interruption on AlSi10Mg alloy processed with L-PBF, and examines the tensile properties and material microstructures. The material properties related to metal welding supported by the L-PBF process are analyzed in [11], where the authors use the AM process to hold a strain sensor in the metal part without additional adhesives.

Initial attempts to integrate sensors into AM parts focused on optical fibers [12], likely due to their thin profile that has relatively low impact on process interruption. In [13], optical fibers were integrated into stainless steel parts for temperature and strain measurements. The fibers were placed into grooved housings and then covered with additional powder layers melted on top. Similar sensors were previously considered in [1]. The integration of optic fibers for sensing purposes in polymers is presented in [14]. The process, called additive layer manufacturing (ALM), is applied to polyamide materials (PA 2200 and PA 3200 GF), and is interrupted and restarted after sensor placement.

The development and production of metal prototypes with integrated sensors remains limited. In 2016, piezoelectric actuators were integrated into monolithic metallic housings produced with L-PBF by [15] to enable smart control of large truss structures. The prototype was also supported by numerical simulations of damped active struts. The integration of sensors and electronics using ultrasonic additive manufacturing (UAM) is presented by [16]. The authors describe the integration of a previously encapsulated sensor into metal parts by welding a thin foil with a sonotrode. They claim that the low temperature of this process preserves the integrity of the sensing element. The author of this paper previously developed and patented a custom process for integrating sensors during the L-PBF process of metals [17], [18]. The same method was used to embed thermal sensors into steel parts [19], [20], [21], based on previous studies of the L-PBF process [22], [23]. In [11], a strain gauge is integrated into the part during the L-PBF metalworking process. This method can theoretically replace the traditional application of strain sensors to metal parts. In [24], eddy current sensors were embedded into L-PBF components for structural monitoring and validated through monitoring of a crack growth process. The material utilized in the study is 316L steel. To integrate the sensor, the process is interrupted and the sensor is placed within a cylindrical cavity with a diameter of 5

mm. The cavity is then sealed with an overhanging surface, and the sensor is secured using a hardening resin. However, the effect of process interruption on the material strength is not investigated. In [25] and [26], the authors demonstrate the validation of process interruption for integrating separate structures with a bridge shape. The external structure can function as a force sensor by utilizing previously attached strain gauges on the bridge. The method validates the structural strength at bridge connections with 316L steel.

This paper presents a methodology for integrating sensors and electronics into L-PBF metal components. The additive process is interrupted to allow for sensor positioning, and the integrity of the material structure is assessed using micrographs. Mechanical strength is measured via tensile tests on dedicated samples, although these analyses are beyond the scope of this work and are not documented here. The customized L-PBF process is then employed to fabricate a sensorized brake caliper. The caliper shape is optimized prior to fabrication to reduce weight and building time, including the positioning of sensor and cables. FEM simulations are used to calculate the global stress distribution under maximum braking torque. The main advantages of the proposed technology are the protection of the sensor against disturbances and dust, strategic positioning of the sensor relative to the measuring point (1 mm from the piston housing), insensitivity to environmental thermal effects, and elimination of conversion algorithms between nominal (at sensor position) and effective (at target position) measurements.

2 METHODOLOGY

The modified L-PBF process involves temporarily interrupting the growth of the part and introducing a "foreign" body into the process. To perform this operation, as shown in Fig. 1, it is crucial to:

a) accurately simulate the time required to grow the core element (1) to the desired size for subsequent operations, without any waiting time that could result in surface oxidation or loss of adhesion for subsequent micromelted layers;
b) disable process parameters associated with downskin surfaces that are automatically applied to suspended parts. In this case, the software ignores the presence of the cover (3) and automatically starts building the upper sealing (4) as a suspended part with downskin setup. However, the upper sealing (4) is not suspended and instead leans on the cover (3).

The fabrication process was interrupted at a height of 17.8 mm after an estimated build time of 9 hours. The entire job duration, including manual operations and time to restore the chamber atmosphere, is estimated to be 12 hours. The following operations were required to build the integrated system:

- Building, releasing, and tooling of the cover element (3).
- Uploading a CAD file, including the core element (1) and the upper sealing (4), to the AM system.
- Building the core element (1) and interrupting the job at the upper surface of (1).
- Opening the building chamber.
- Cleaning the powder inside and around the core (1).

- Positioning the sensor, cable, and connector (2) into the core housing (1).
- Applying the previously fabricated cover (3).
- Restoring the powder planarity around the assembly.
- Closing the building chamber.
- Restoring the controlled atmosphere into the chamber.
- Restarting the micromelting process and building the upper sealing (4).

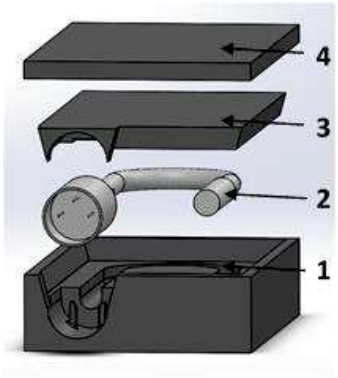

Figure 1: Schematics of the integration sequence: core element (1), sensor with cable and connector (2), cover element (3), upper sealing (4).

3 PROCESS VALIDATION

The preliminary activity involves validating the integration process described above by incorporating a thermal sensor into a 17-4 PH steel square sample measuring 88x55x25 mm^3. The AM system used for this purpose is EOS M270 (building volume of 250x250x215 mm^3, Yb-fiber laser of 200 W, system power of 5.5 kW, building speed in the range of 2-20 mm^3/s, maximum scan speed of 7.0 m/s, and layer thickness of 20-100 μm). The powder used in this process has particles within the size range of 36-44 μm (D50 according to ASTM B822), with a maximum of 6.0% wt. of particles > 53 μm (ASTM B214) and 1.0% wt. of particles > 63 μm (ASTM B214), and a mean apparent density of 3.83 g/cm^3 (ASTM B212) and mean tap density of 4.7 g/cm^3 (ASTM B527). The printing parameters used are as follows [27]: 40 μm layer thickness, 200 W laser power, 25 mm/min scanning speed, and 11 μm scanning spacing.

3.1 Cover element

The mechanical coupling of the core element (1) and the cover element (3) is critical in achieving planarity of the cover's upper surface after coupling. If the planarity is low or there are residual steps between (1) and (3), the process restart may fail or induce geometrical defects. The powder distributor, also known as the "re-coater," is designed to work on perfectly planar surfaces. A uniform powder layer on the assembly is necessary for further micromelting.

To ensure perfect coupling between (1) and (3), the dimensional tolerance of the cover element (3) must be accurately defined. For this purpose, several cover element variants with slightly different widths are fabricated, as shown in Fig. 2: nominal size (43 mm), ±0.05 mm

deviation, and ±0.10 mm deviation. The best fitting is found during the manual operation on the job. In this case, the preferred version of the cover is the one with a 43+0.10 mm deviation.

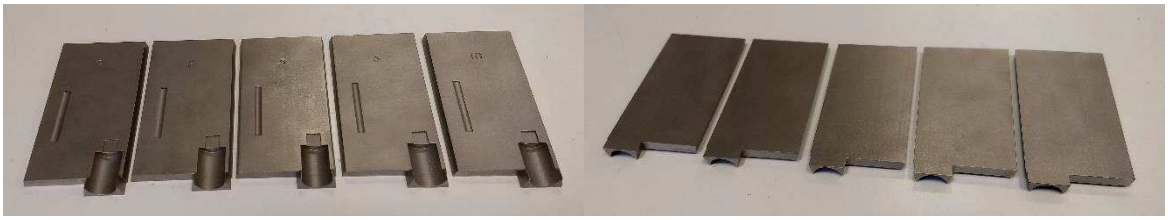

Figure 2: Cover elements with different tolerance of the nominal width: 43 mm, ±0.05 mm deviation, and ±0.10 mm deviation.

3.2 Thermal sensor

The thermo-resistive sensor used is a class A PT100 sensor. It is housed in a 6 mm diameter AISI316 steel casing and is connected electrically via a cable with silicon coating and three conductors. The sensor follows the ITU-90 standard thermo-electric characteristic (simplified for temperatures above 0°C), which is expressed by the equation:

$$R_t = R_0 \cdot (1 + At + Bt^2) \tag{1}$$

where t is the temperature, R_t is the resistance at temperature t, R_0 = 100 Ω (resistance at 0°C), and the other coefficients are A = $3.9083 \cdot 10^{-3}$ and B = $-5.7750 \cdot 10^{-7}$. The temperature can be calculated using the equation

$$t = \frac{-R_0 A + \sqrt{R_0^2 A^2 - 4R_0 B(R_0 - R_t)}}{2R_0 B} \tag{2}$$

3.3 Sensor and connector preparation

Before starting the process, the sensor, cable, and connectors need to be prepared. The cable length must be accurately measured according to the housing size built inside the core element (1). In this case, the cable length required is 125 mm. The male connector is soldered to the cable using tin. Heat-shrink sleeves are used to insulate the electrical connections. The cable is provided with a silicone-based sleeve by the manufacturer to protect against high temperatures. The electrical assembly is then dimensionally checked using a simulator that reproduces the exact geometry of the further part (Fig. 3).

3.4 Electric connector

The component features a multipolar connector on its surface, which allows for external cables to be easily connected. The male connector is securely installed onto the component to prevent separation during operation, using two anchors that engage with the metal part (Fig. 4).

Once the connector is applied to the assembly, it needs to be protected from damage during the micromelting process restart or the release of the part after the additive process. Additionally, the water used as a lubricant in wired electroerosion must be kept away from the electrical components. To achieve this, a specific protection is applied.

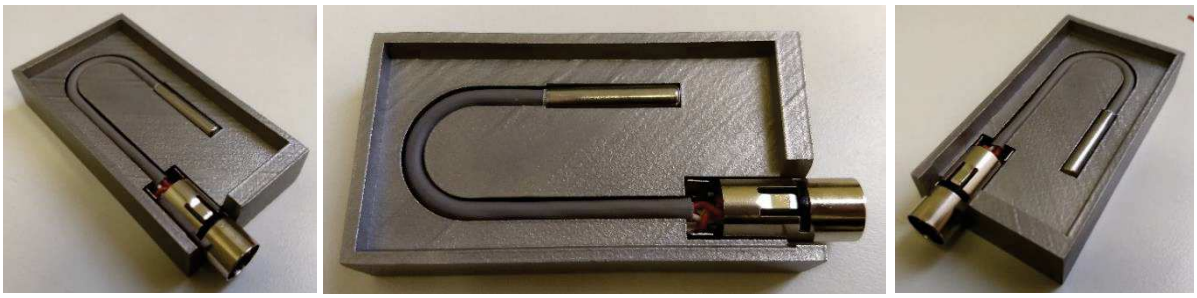

Figure 3: Installation of the sensor with cable and connector into the simulator reproducing the core element.

a) 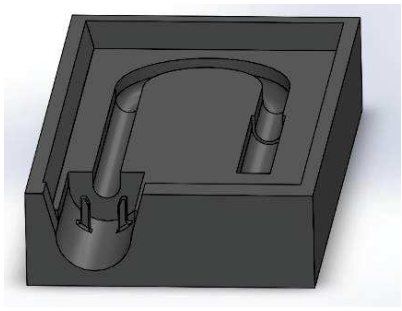 b) 

Figure 4: Core element with vertical anchors for connector holding (a), connector placed into the housing (b).

3.5 Building process

The process steps described above are presented in Fig. 5 below.

a)  b) 

c) 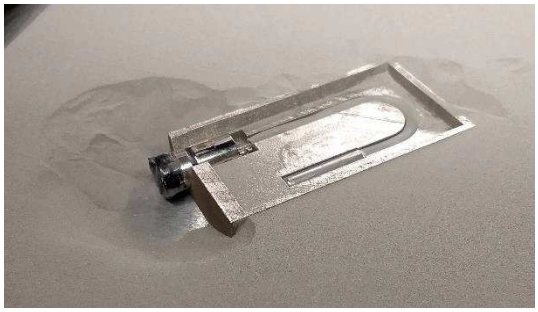 d) 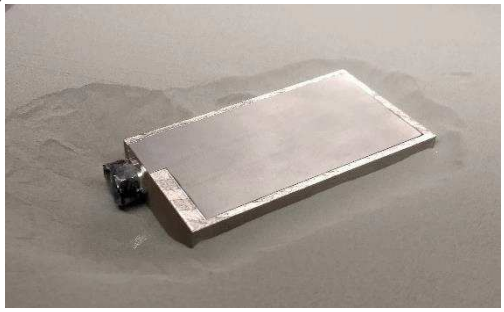

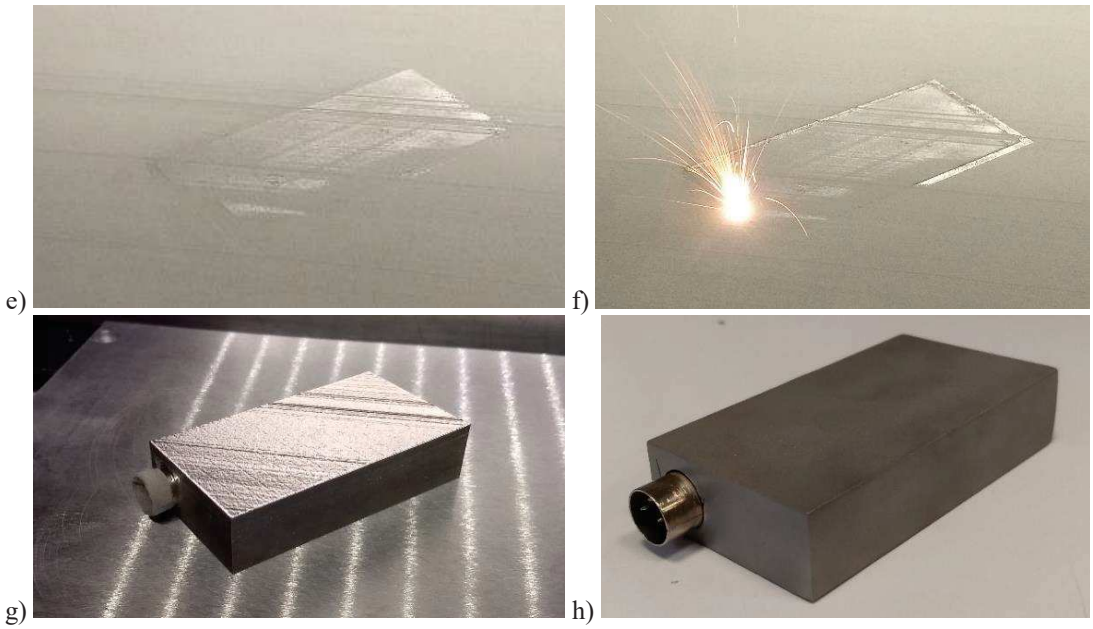

Figure 5: Fabrication process steps. Fabrication of the core element before the interruption (a), interruption layer at 17.8 mm (b), powder cleaning inside the core element and application of the electrical assembly (c), application of the cover (d), restore of the powder planarity (e), micromelting restart and building of the upper sealing (f), end of the process and powder removal (g), final part after release and surface finishing (h).

4 BRAKE CALIPER WITH EMBEDDED THERMAL SENSOR

The described integration methodology is then applied to fabricate a brake caliper, which represents a case study of a real application device.

4.1 Structural design

The mechanical design of the structural parts of the brake caliper is optimized for AM. The design optimization is based on calculating the braking torque specification with reference to the system shown in Fig. 6a. The operative conditions of a typical braking test for racing bikes [28] are applied, which include a 180 mm braking disc (effective braking radius r_{eff} = 83 mm) and C_f = 166 Nm torque (including a safety factor of 2), corresponding to a 40 N force on the braking leverage. The tangent force F_t between the brake pads and the disc is determined by:

$$t = \frac{!"}{\#\$""} = 2000\,\text{N} \tag{3}$$

The normal braking force is then calculated as:

$$\&' = \frac{\&t}{(} = 4444\,\text{N} \tag{4}$$

where the friction coefficient $*_d$ = 0.45 has been estimated to be in agreement with typical braking disc performances [29], although this value may change depending on the brake pad's

wearing conditions and temperature. According to the relationship + = &, / , , the values A = 823 mm^2 and p = 5.4 MPa are assigned to the overall piston area and oil pressure, respectively. Two coupled pistons with diameters d_1 = 17.20 mm and d_2 = 15.10 mm are used in the caliper.

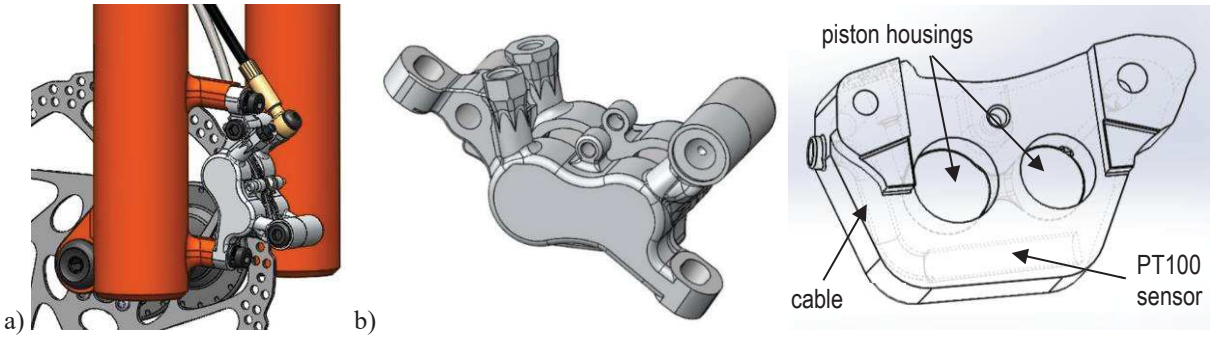

Figure 6: Structural model of the brake caliper: applied to braking system (a), optimized geometry (b).

The component's final shape is optimized using Inspire software and the PolyNURBS function, and free-form reshaping techniques. The FEM model consists of structural elements with an average size of 0.4 mm. The metal structure's final mass is 215 g. The maximum Von Mises stress, excluding local discretization effects, is 170 MPa, and the maximum displacement is 0.07 mm, according to the FEM simulation.

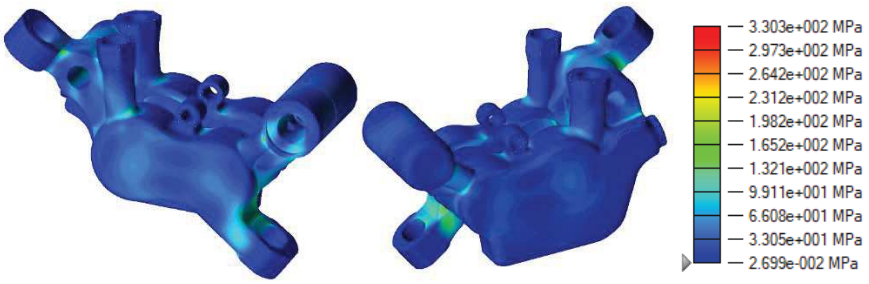

Figure 7: Von Mises equivalent stress on the caliper from FEM modeling.

4.2 Fabrication and tooling

Temporary supports were added to enable the part to be held on the milling machine (Fig. 8). Some functional regions (in blue) have been mechanically processes: pistons housings, threats, planarity of coupled surfaces. The final component after tooling operations is shown in Figs. 9a-9b. The assembled caliper, including sealing, pistons, oil pipe, braking pads, springs, and screws, is shown in Fig 9c. The circuit is then filled with oil at the nominal pressure, and the air is extracted.

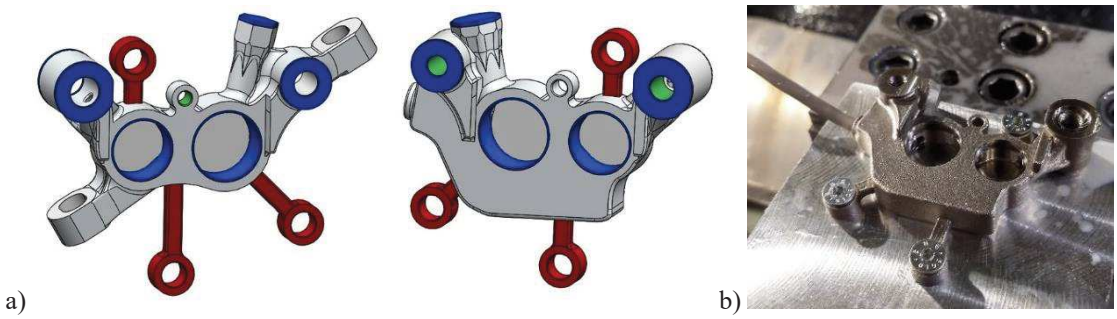

Figure 8: Temporary supports for holding the part in milling operations: design (a) and tooling (b).

Figure 9: Brake caliper after mechanical tooling (a, b) and in the final assembled configuration (c).

4.3 Sensing performances validation

The braking system has been installed on a racing bike for functional validation. The bike is then mounted on rolling supports typically used for indoor training. The operator rotates the rear wheel and activates the brake from the manual lever on the handlebar. The braking action generates thermal heating of the pads due to friction with the disc. The thermal conduction also causes the heating of the metal case around the piston housings. The thermal sensor is used to measure local heating and provide real-time brake diagnostics. Under normal conditions, uncontrolled heating may cause oil temperature to increase and result in loss of performance. In racing conditions, external air flow against the caliper may disrupt external measurements. The embedded sensor, on the other hand, is designed to provide local detection close to the heating point with minimal external disturbances. The validation setup includes the National Instruments digital multimeter VB-8012 and the LabView software interface.

The following tests have been conducted:

- application of uniform braking force to the lever while the rear wheel is rotating at high speed; uniform heating is expected (Test 1 and Test 2);
- application of a sequence of braking forces to the lever, separated by pedal actions to restore the initial speed; heating and cooling sequence is expected (Test 3).

The PT100 sensor conversion curve is utilized to convert the electrical output signal into temperature information. The results are shown in Fig. 10. The measured curves are consistent with the anticipated trends. For all tests, the initial ambient temperature is in the range of 24-

27°C. The maximum temperatures detected by the embedded sensing system range between 56 and 61°C.

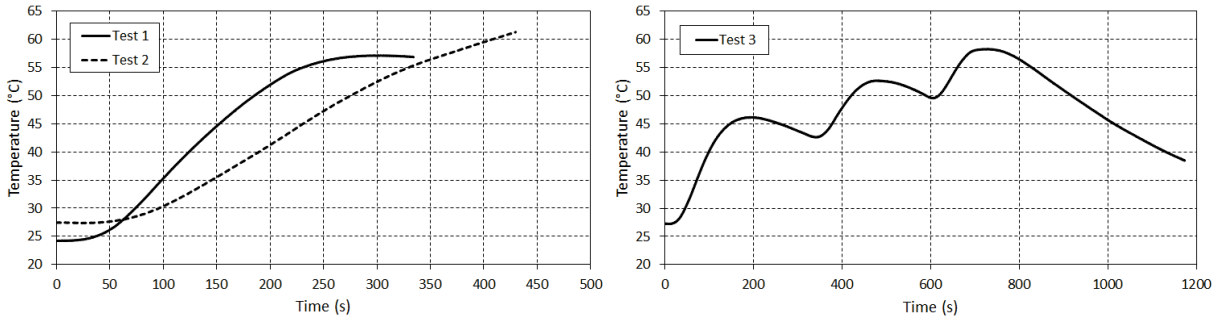

Figure 10: Experimental validation of sensing performance of the integrated sensor under uniform braking force (left) and under a sequence of several braking forces (right).

5 CONCLUSIONS

The methodology based on customized L-PBF process that is suitable for the integration of sensors and electronics into AM metal parts has been demonstrated. The qualitative result of the process is highly satisfactory in terms of material integrity of the components, preservation of electronic functionality, integration of process steps, and overall process time. The functionality of the components is improved through the application of the presented method, particularly regarding the protection and insulation of the sensor, cable, and connector, the optimized positioning of the sensor, and the insensitivity to external contamination and interferences. Moreover, the customized process described can be implemented at an industrial scale with partial or total automation of the pick and place steps.

REFERENCES

[1] X. Li, "Embedded sensors in layered manufacturing," PhD thesis, Stanford University, Stanford, CA, 2001.

[2] D. Lehmhus, C. Amund-Kopp, F. Petzoldt, D. Godlinski, A. Haberkorn, V. Zöllmer, and M. Busse, "Customized smartness: a survey on links between additive manufacturing and sensor integration," *Procedia Technology*, vol. 26, 284-301, 2016.

[3] T. Vasilevitsky and A. Zoran, "Steel-Sense: integrating machine elements with sensors by additive manufacturing," In Proc. *Conference on Human Factors in Computing Systems (CHI '16)*, 2016, pp. 5731-5742.

[4] T. Töppel, H. Lausch, M. Brand, E. Hensel, M. Arnold, and C. Rotsch, "Structural integration of sensors/actuators by laser beam melting for tailored smart components," *Additive Manufacturing of Composites and Complex Materials*, vol. 70, no. 3, pp. 321-327, 2018.

[5] M. Binder, L. Kirchbichler, C. Seidel, C. Anstaett, G. Schlick, and G. Reinhart, "Concepts for the integration of electronic components into metal laser-based powder bed fusion parts," In Proc. *52nd CIRP Conference on Manufacturing Systems*, 2019, pp. 992-997.
[6] M. Binder, C. Anstaett, R. Reisch, G. Schlick, C. Seidel, and G. Reinhart, "Automated manufacturing of mechatronic parts by laser-based powder bed fusion," *Procedia Manufacturing*, vol. 18, pp. 12-19, 2018.
[7] M. Binder, M. Illgner, C. Anstaett, P. Kindermann, L. Kirchbichler, and C. Seidel, "Automated manufacturing of sensor-monitored parts," Laser Technik Journal, vol. 3, pp. 36-39, 2018.
[8] M.S. Hossain, J. Mireles, P. Morton, Y. Lin, C.A. Terrazas, and R.B. Wicker, "Part re-registration during process interruption of electron beam melting additive manufacturing," *The International Journal of Advanced Manufacturing Technology*, vol. 96, pp. 337-344, 2018.
[9] P. Stoll, A. Spierings, and K. Wegener, "Impact of a process interruption on tensile properties of SS 316L parts and hybrid parts produced with selective laser melting," *The International Journal of Advanced Manufacturing Technology*, vol. 103, pp. 367-376, 2019.
[10] M. Binder, C. Leong, C. Anstaett, G. Schlick, C. Seidel, and G. Reinhart, "Effects of process interruptions on the microstructure and tensile properties of AlSi10Mg parts manufactured by laser-based powder bed fusion," *Procedia CIRP*, vol. 94, pp. 182-187, 2020.
[11] M. Binder, M. Fischer, S. Dietrich, C. Seidel, and G. Reinhart, "Integration of strain gauges in components manufactured by laser-based powder bed fusion," In Proc. *20th Machining Innovations Conference for Aerospace Industry (MIC '20)*, 2020, pp. 1-8.
[12] N. Saheb and S. Mekid, "Fiber-embedded metallic materials: from sensing towards nervous behavior," *Materials*, vol. 8, no. 11, pp. 7938-7961, 2015.
[13] D. Havermann, J. Mathew, W.N. MacPherson, R.R.J. Maier, and D.P. Hand, "Temperature and strain measurements with fiber Bragg gratings embedded in stainless steel 316," *Journal of Lightwave Technology*, vol. 33, no. 12, pp. 2474-2479, 2015.
[14] R.R. Maier, W.N. MacPherson, J.S. Barton, M. Carne, M. Swan, J.N. Sharma, S.K. Futter, D.A. Knox, B.J.S. Jones, and S. McCulloch, "Embedded fiber optic sensors within additive layer manufactured components," *IEEE Sensors Journal*, vol. 13, no. 3, pp. 969-979, 2013.
[15] D. Mayer, H.A. Stoffregen, O. Heuss, J. Thiel, E. Abele, and T. Melz, "Additive manufacturing of active struts for piezoelectric shunt damping," *Journal of Intelligent Material Systems and Structures*, vol. 27, no. 6, pp. 743-754, 2016.
[16] A. Bournais-Varotsis, X. Han, R.A. Harris, and D.S. Engstrøm, "Ultrasonic additive manufacturing using feedstock with build-in circuitry for 3D metal embedded electronics," *Additive Manufacturing*, vol. 29, pp. 100799, 2019.
[17] G. De Pasquale and M. Romeo, "Metodo per realizzare un sistema di misura integrato in un componente ottenuto da microfusione di polveri," Italian Patent 201800005012, 2 May, 2018.

[18] G. De Pasquale and M. Romeo, “Method for implementing a measurement system embedded in a component obtained by powder micro-melting,” WO/2019/211779, 7 Nov 2019.
[19] G. De Pasquale, A. Buffon, and L. Bongiorni, “Sensors integration in additive DMLS metal parts,” *Transactions on Additive Manufacturing Meets Medicine (AMM)*, vol. 2, no. 1, 2020.
[20] G. De Pasquale, L. Bongiorni, and A. Buffon, “Componenti in lega metallica con sensori ‘nativi’,” *Organi di Trasmissione*, pp. 24-27, 2021.
[21] G. De Pasquale, “Thermal sensing of AM components through electronics embedding in LB-PBF process,” In Proc. *International Conference on Nonlinear Solid Mechanics (ICoNSoM ’22)*, pp. 105-106, 2022.
[22] G. De Pasquale, F. Luceri, and M. Riccio, “Experimental evaluation of selective laser melting process for optimized lattice structures,” *Proc IMechE Part E: Journal of Process Mechanical Engineering*, vol. 233, no. 4, pp. 763-775, 2019.
[23] G. De Pasquale, F. Luceri, and M. Riccio, “Experimental characterization of SLM and EBM cubic lattice structures for lightweight applications,” *Experimental Mechanics*, vol. 59, pp. 469-482, 2019.
[24] P. Stoll, E. Gasparin, A. Spierings, and K. Wegener, “Embedding eddy current sensors into LPBF components for structural health monitoring,” *Progress in Additive Manufacturing*, vol. 6, pp. 445-453, 2021.
[25] R. Chadda, J. Probst, C. Hartmann, M. Link, M. Hessinger, E. Abele, M. Weigold, and M. Kupnik, "Disruptive force sensor based on laser-based powder-bed-fusion," In Proc. *IEEE Sensors*, 2020, pp. 1-4.
[26] R. Chadda, M. Link, T. Engel, C. Hartmann, O.Ben Dali, J. Probst, H. Merschroth, E. Abele, and M. Weigold, “Evaluation of additively manufactured parts in disruptive manner as deformation elements for structural integrated force sensors," *IEEE Sensors Journal*, vol. 22, no. 20, pp. 19249-19258, 2022.
[27] L. Huang, Y. Cao, H. Zhao, Y. Li, Y. Wang, and L. Wei, “Effect of process parameters on density and mechanical behaviour of a selective laser melted 17-4PH stainless steel alloy,” *Open Physics*, vol. 20, no. 1, pp. 66-77, 2022.
[28] T. Worsey, “The best MTB disc brake you can buy,” Enduro Mountainbike Magazine, *enduro-mtb.com*, Jun. 6, 2018. [Online]. Available: https://enduro-mtb.com/en/best-mtb-disc-brake-can-buy/. [Accessed March 28, 2023].
[29] C. Oertel, H. Neuburger, and A. Sabo, “Construction of a test bench for bicycle rim and disc brake,” *Procedia Engineering*, vol. 2, pp. 2943-2948, 2010.